Publication Year	2016
Acceptance in OA	2020-05-13T07:15:46Z
Title	Chandra Observation of Abell 1142: A Cool-core Cluster Lacking a Central Brightest Cluster Galaxy?
Authors	Su, Yuanyuan, Buote, David A., GASTALDELLO, FABIO, van Weeren, Reinout
Publisher's version (DOI)	10.3847/0004-637X/821/1/40
Handle	http://hdl.handle.net/20.500.12386/24763
Journal	THE ASTROPHYSICAL JOURNAL
Volume	821

The Astrophysical Journal, 821:40 (11pp), 2016 April 10
doi:10.3847/0004-637X/821/1/40

CHANDRA OBSERVATION OF ABELL 1142: A COOL-CORE CLUSTER LACKING A CENTRAL BRIGHTEST CLUSTER GALAXY?

Yuanyuan Su[1,2], David A. Buote[2], Fabio Gastaldello[3], and Reinout van Weeren[1]
[1] Harvard-Smithsonian Center for Astrophysics, 60 Garden Street, Cambridge, MA 02138, USA; yuanyuan.su@cfa.harvard.edu
[2] Department of Physics and Astronomy, University of California, Irvine, 4129 Frederick Reines Hall, Irvine, CA 92697, USA
[3] INAF-IASF-Milano, Via E. Bassini 15, I-20133 Milano, Italy

Received 2015 November 10; accepted 2016 February 15; published 2016 April 6

ABSTRACT

Abell 1142 is a low-mass galaxy cluster at low redshift containing two comparable brightest cluster galaxies (BCGs) resembling a scaled-down version of the Coma Cluster. Our *Chandra* analysis reveals an X-ray emission peak, roughly 100 kpc away from either BCG, which we identify as the cluster center. The emission center manifests itself as a second beta-model surface brightness component distinct from that of the cluster on larger scales. The center is also substantially cooler and more metal-rich than the surrounding intracluster medium (ICM), which makes Abell 1142 appear to be a cool-core cluster. The redshift distribution of its member galaxies indicates that Abell 1142 may contain two subclusters, each of which contain one BCG. The BCGs are merging at a relative velocity of $\approx$1200 km s^{-1}. This ongoing merger may have shock-heated the ICM from $\approx$2 keV to above 3 keV, which would explain the anomalous L_X–T_X scaling relation for this system. This merger may have displaced the metal-enriched "cool core" of either of the subclusters from the BCG. The southern BCG consists of three individual galaxies residing within a radius of 5 kpc in projection. These galaxies should rapidly sink into the subcluster center due to the dynamical friction of a cuspy cold dark matter halo.

Key words: dark matter – galaxies: clusters: individual (Abell 1142) – galaxies: clusters: intracluster medium – galaxies: individual (NGC 3492, IC 664) – galaxies: ISM

1. INTRODUCTION

X-ray observations reveal two populations of galaxy clusters: cool-core clusters (CC) and non-cool-core clusters (NCC). CC clusters possess a sharp X-ray emission peak with a positive radial temperature gradient due to the radiative cooling of its dense core (e.g., Molendi & Pizzalato 2001; Sanders et al. 2004; Sanderson et al. 2006). The metal distribution in the intracluster medium (ICM) of CC clusters peaks at the cluster center, which further enhances the cooling process (e.g., De Grandi & Molendi 2001, Ettori et al. 2015). In contrast, the gaseous, thermal, and chemical distributions of NCC clusters are relatively homogenous. Cosmological simulations also reproduced the metallicity and temperature profiles of CC clusters, which are steeper than those of NCC clusters (e.g., Rasia et al. 2015).

A fundamental question is whether CC and NCC are formed intrinsically differently or whether any cluster can transform into either type over cosmic time. Cavagnolo et al. (2009) found that the central entropy of galaxy clusters is bimodal with two distinct peaks at 15 and 150 keV cm^2 respectively. Non-gravitational preheating may have increased the entropy of NCC clusters to above 300 keV cm^2, and they never had enough time to develop a cool core. This difference may also be set by different levels of conduction. A critical entropy threshold (30–50 keV cm^2) may exist, only below which can conduction be halted and a cool-core form (Guo et al. 2008; Voit et al. 2008).

Meanwhile, many scenarios have been proposed arguing against a primordial origin of the CC/NCC dichotomy. Heating from active galactic nuclei (AGNs) and their associated bubbles may counteract radiative cooling at the cluster center (e.g., McNamara & Nulsen 2007; Guo & Mathews 2010; Fabian 2012). If CC and NCC clusters are distinguished by their central AGN activity, then it would not explain why CC clusters are more relaxed than NCC clusters. However, observations show that most CC clusters appear to be more symmetric than NCC clusters (Buote & Tsai 1996; Sanderson et al. 2009). These results favor major mergers as the origin of NCC clusters. Major mergers may have wiped out nascent cool cores in NCC clusters, while CC clusters experience only minor mergers and preserve their cool cores (Burns et al. 2008; Henning et al. 2009). In principle, all NCC clusters will eventually evolve into CC clusters given enough time to relax (McGlynn & Fabian 1984; Buote 2002). Nevertheless, Motl et al. (2004) proposed that mergers may even transform NCC clusters into CC clusters with cold gas supplied by infalling subgroups.

As the largest gravitationally bound objects in the universe, galaxy clusters are able to retain the bulk of metals synthesized by supernovae. The metal abundance ratios in the ICM and their spatial distributions provide important clues to the chemical enrichment history and formation process of galaxy clusters. Previous X-ray observations of groups and clusters indicate a centrally peaked Fe profile coupled with a relatively homogenous distribution of O and Si (e.g., Finoguenov et al. 2000; Buote 2001; Bohringer & Werner 2010; Sanderson & Ponman 2010). This implies that α-elements have been supplied during the pre-enrichment phase by young, massive stars through Type II supernovae (SNe II), while most Fe has been ejected into the ICM more recently by the central brightest cluster galaxy (BCG) through Type Ia supernovae (SNe Ia). However, a few studies using *Chandra* or *XMM-Newton* observations report an Si distribution just as centrally peaked as that of Fe (e.g., Buote et al. 2003; Simionescu et al. 2010; Million et al. 2011). The cluster center may be more enriched by SNe II than previously thought, which challenges our understanding of the history of galaxy clusters. Elkholy et al. (2015) measured a larger scatter in the central Fe mass among low-mass clusters relative to high-mass clusters. They interpret this as more frequent mergers (mixing) of subgroups in larger clusters, resulting in a more constant metal content. Metal-rich gas from an infalling galaxy or sub-group has been seen to reach the cluster center in some simulations (e.g., Cora 2006), which explains the observed SN II products at the cluster center. It is unclear whether the central metal excess in the ICM is due to the BCG or due to the infall of metal-rich gas. An ideal test is to study the central metal content of a galaxy cluster without a BCG at its X-ray center. Unfortunately, most such systems are NCC clusters that lack a metal abundance gradient, likely having had their central metal peak destroyed by cluster mergers (e.g., De Grandi & Molendi 2001; Matsushita 2011).

Abell 1142, presented in this paper, is a poor cluster cataloged in the Northern *ROSAT* All-Sky galaxy cluster survey (Bohringer et al. 2000) with an X-ray luminosity of $L_X = 2.8 \times 10^{43}$ erg s^{-1} in the 0.1–2.4 keV band. Rather than having a definitive BCG, it contains two bright galaxies (indicated by G1 and G2 in Figure 1). Lin & Mohr (2004) take G1 (NGC 3492; $z = 0.036$; galaxy pair) as the BCG, while Abdullah et al. (2011) take G2 (IC 664; $z = 0.034$; S0) as the BCG. As demonstrated below, the ICM of Abell 1142 harbors a cool core detached from either BCG. Abell 1142 provides us with an opportunity to study a "cool core" in the absence of a BCG as well as the role of the BCG in the cluster enrichment process. In this work, we report our *Chandra* analysis of Abell 1142.

We assume a luminosity distance of 152 Mpc for Abell 1142 based on a redshift of $z = 0.035$ taken from the NASA/IPAC Extragalactic Database (NED). A cosmology with $H_0 = 70$ km s^{-1} Mpc^{-1}, $\Omega_\Lambda = 0.7$, and $\Omega_m = 0.3$ was adopted, corresponding to a linear scale of $1' = 41.3$ kpc at the assumed distance. All uncertainty ranges are 68% confidence intervals (1σ), unless stated otherwise.

2. OBSERVATIONS AND DATA REDUCTION

2.1. *Chandra*

Abell 1142 was observed with *Chandra* for 27 ks on 2006 January 17 (ObsID: 06938). The aimpoint was on the back-side illuminated ACIS-S3 CCD. The standard *Chandra* data processing package *CIAO* 4.7 and the *Chandra* calibration database (*CALDB*) 4.6.9 were used to process and analyze the data. The observation was reprocessed from level 1 events using the *CIAO* tool `repro`. CTI and time-dependent gain corrections were applied. Bad pixels, bad columns, and node boundaries were discarded. Background flares beyond 3σ was filtered with the light-curve filtering script `lc_clean`. The entire 27 ks observation was fairly quiescent. We identified point sources in the 0.3–7.0 keV energy band using `wavdetect`; a 2.0 keV exposure map was supplied. The detection threshold was set at 10^{-6} and the scales ranged from 1 to 8, in steps increasing by a factor of $\sqrt{2}$.

2.1.1. *Imaging Analysis*

We generated images in eight energy bands: 0.5–0.8 keV, 0.8–1.2 keV, 1.2–1.5 keV, 1.5–2.0 keV, 2.0–2.5 keV, 2.5–3.0 keV, 3.0–3.5 keV, and 3.5–4.0 keV. We normalized these images with monochromatic exposure maps defined at the central energy of each band. For each image, we subtracted an estimate of the background using the blank-sky fields available in the *Chandra* calibration database (CALDB). The background level was normalized by its count rate in 9.5–12.0 keV relative to the observation. We filled point sources with pixel values interpolated from surrounding background regions using `dmfilth`. A final 0.5–4.0 keV image was produced by adding all eight of these narrow-band images. We further adaptively smoothed the image using `dmimgadapt`, as shown in Figure 1.

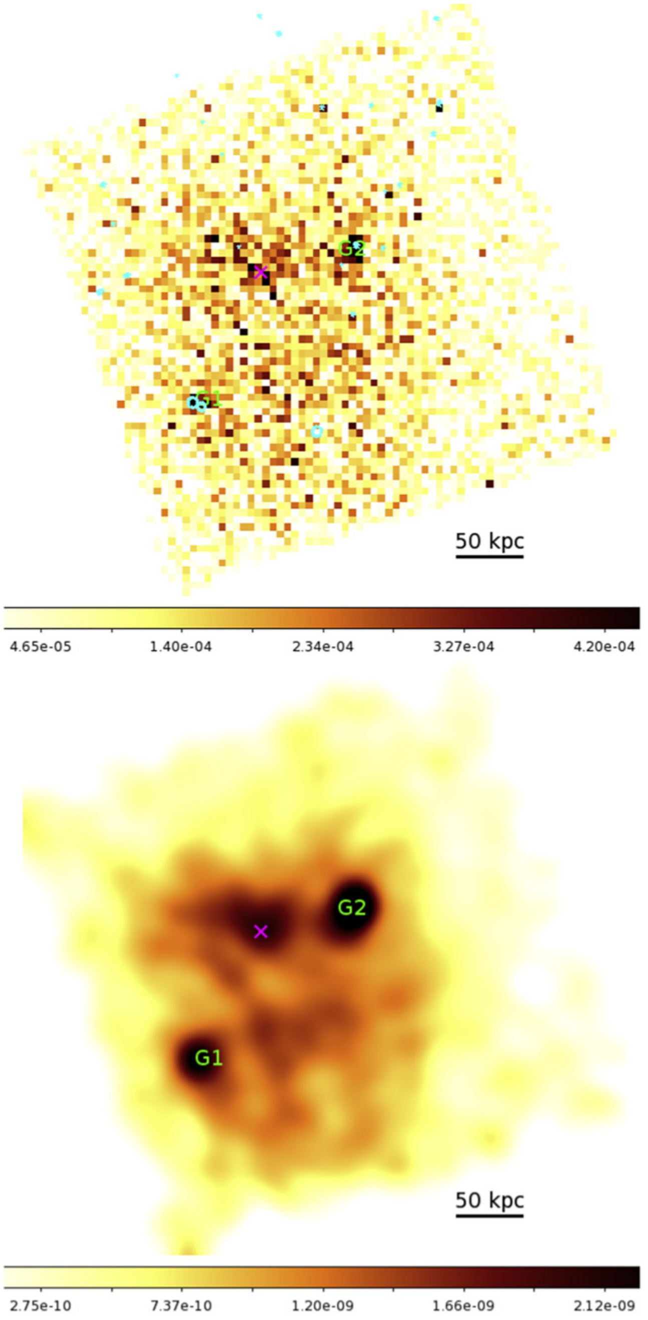

Figure 1. 27 ks exposure-corrected and blank-sky background subtracted *Chandra* ACIS-S image of Abell 1142 and in the energy band of 0.5–4.0 keV. Top: the image was binned by 16 × 16 pixels in units of counts s^{-1}. Positions of point sources were marked in cyan ellipticals. Bottom: adaptively smoothed in units of photon cm^{-2} s^{-1}. Locations of G1 and G2 are indicated. The peak of cluster gas emission is indicated by the magenta cross.

The distribution of the hot gas is very diffuse without a dominant central emission peak, but instead possesses multiple peaks of modest intensity. The X-ray emission contours reveal

Table 1
Best Fits and Background Systematics

		Annulus 1		Annulus 2		Annulus 3		Annulus 4	
Temperature	best fit	$1.85^{+0.24}_{-0.20}$		$3.34^{+0.5}_{-0.28}$		$3.05^{+0.3}_{-0.2}$		$2.52^{+0.49}_{-0.67}$	
	Δ Particle	−0.03 (−0.01)		−0.03 (+0.01)		−0.05 (+0.01)		−0.04 (+0.07)	
(keV)	Δ X-ray	−0.01 (−0.01)		+0.01 (+0.03)		−0.01 (+0.01)		−0.01 (+0.04)	
Metallicity	best fit	$0.67^{+0.4}_{-0.2}$		$0.57^{+0.24}_{-0.17}$		…		$0.14^{+0.14}_{-0.12}$	
	Δ Particle	−0.01 (+0.01)		−0.03 (+0.04)		…		+0.02 (+0.01)	
($Z_\odot$)	ΔX-ray	+0.03 (−0.02)		+0.01 (−0.02)		…		+0.01 (−0.02)	
		ann 1	ann 2	ann 3	ann 4	ann 5	ann 6	ann 7	ann 8
Hardness	best fit	0.14 ± 0.05	0.18 ± 0.05	0.22 ± 0.06	0.2 ± 0.05	0.2 ± 0.04	0.21 ± 0.05	0.26 ± 0.06	0.24 ± 0.04
Ratio	Δbackground	±0.02	±0.02	±0.03	±0.03	±0.03	±0.04	±0.05	±0.05

Note. We increase (decrease) the best-determined particle and X-ray backgrounds by 5% and 10%, respectively, for the spectral analyses. We varied the level of blank sky by 5% for the hardness ratio measurements. The background systematic uncertainties are smaller than the statical uncertainties. Best fits are plotted in Figure 2.

three peaks (labeled as G1, G2, and X), offset by ∼100–200 kpc from each other. Peaks G1 and G2 overlap with the BCGs G1 and G2, respectively, while Peak X does not correspond to any large galaxy. The count rate (within 20 kpc) of Peak X ($0.01\,\mathrm{cts\,s^{-1}}$) is comparable those of Peak G1 ($0.007\,\mathrm{cts\,s^{-1}}$) and Peak G2 ($0.012\,\mathrm{cts\,s^{-1}}$). We adopt Peak X as the "center" of the cluster for the following analyses since it lies roughly midway between G1 and G2, closer to the ICM center.

2.1.2. Spectrum Analysis

Individual spectra were extracted from four concentric circular regions centered on Peak X: 0″–65″, 65″–123″, 123″–177″, and 177″–295″. Approximately the same number of net counts were contained in each region and they were just sufficient for spectral analysis. Instrument response files were generated for each spectrum using the CIAO tools `mkwarf` and `mkacisrmf`. The spectral fit was performed in the energy band 0.5–7.0 keV with *XSPEC*12.7. A C-statistic was used to measure the goodness of the fit. The spectra were grouped to have at least 20 photons per energy bin in order to increase computational speed (Humphrey et al. 2009; Su et al. 2015a). All four annuli were fitted simultaneously. Both the cluster emission and background components were modeled.

The X-ray background was approximated by $\mathtt{apec}_{\mathrm{LB}} + \mathtt{phabs} \times (\mathtt{apec}_{\mathrm{MW}} + \mathtt{pow}_{\mathrm{CXB}})$. An `apec` thermal emission model represents the Local Bubble component; an additional `apec` model represents the Milky Way emission (Smith et al. 2001), and a power-law model `pow` ($\Gamma = 1.41$) respresents the unresolved cosmic X-ray background (De Luca & Molendi 2004). The temperatures of the Local Bubble and Milky Way components were fixed at 0.08 and 0.2 keV, respectively. The photoelectric absorption was characterized by the `phabs` model. Photoionization cross-sections were taken from Balucinska-Church & McCammon (1992). The Galactic hydrogen column density was fixed at $N_H = 2.3 \times 10^{20}\ \mathrm{cm}^{-2}$ for Abell 1142, derived from the Dickey & Lockman (1990) map incorporated in the *HEASARC* N_H tool. The particle background was modeled through a number of Gaussian lines and a broken power-law model (see Humphrey et al. 2012; Su et al. 2015a). The background emission of each annulus was forced to have a uniform surface brightness, but the total normalizations were allowed to vary freely.

We used a single thermal `apec` component to model the ICM emission in each annulus. The ICM components were allowed to vary independently for each radial annulus. Since the metallicity is less well constrained than the temperature, we found it necessary to tie together the abundances in annuli 2 and 3. Projected temperature and metal abundance profiles of Abell 1142 are shown in the solid line in Figure 2 and the results are listed in Table 1. To assess the impact of the binning, we also performed the spectral analysis with only three radial bins, as shown by the dashed lines, which indicates similar results.

We produced a hardness ratio map of Abell 1142 using the contour binning analysis developed by Sanders (2006). We generated a contour binning image containing 19 regions for the mosaic image in 0.5–2.0 keV with at least 200 net counts in each bin. We extracted counts in each region from the mosaic image in 0.5–2.0 keV and 2.0–7.0 keV, respectively. We subtracted background components (X-ray background and particle background) from each energy band. We obtained a hardness ratio map using the ratio of counts in the 0.5–2.0 keV to 2.0–7.0 keV bands (see Figure 3). The uncertainties on the hardness ratios are 20%–30%. In the hard band, the background dominates the cluster outskirts regions near the chip edges, for which we did not obtain reasonable and meaningful hardness ratio measurement, and so it was left out from our results. We also derived a hardness ratio profile of eight radial bins ranging from the cluster center out to 4′ shown in green circles in Figure 2 and tabulated in Table 1.

To assess the background systematics, we varied the X-ray background and particle backgrounds by 10% and 5%, respectively, for the spectral analyses. We also varied the level of the blank-sky background by 5% for the hardness ratio measurement. The impacts of these variations are listed in Table 1. Overall, the background systematic uncertainties are smaller than the statistical uncertainties of our results.

2.2. Very Large Array (VLA)

Abell 1142 was observed with the VLA at 1.4 GHz in B-array on 1992 January 12 and in C-array on 1989 June 7 at 1.5 GHz. A total bandwidth of 50 MHz was recorded for both observations. The total on-source times were 6 and 7 minutes for the B- and C-array observations, respectively. The data were reduced and calibrated using CASA version 4.4 (McMullin et al. 2007). The flux-scale was set using the primary calibrator 3C286 with the Perley-Butler 2010 flux-scale. The flux-scale was bootstrapped from the primary to the secondary calibrators and the gain solutions were applied to the

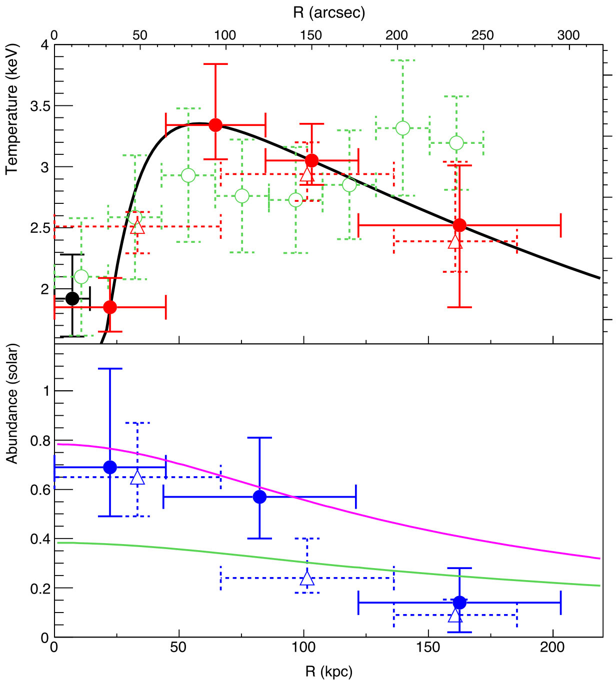

Figure 2. Projected temperature (top) and metal abundance (bottom) profiles of Abell 1142 centered on the X-ray emission peak (four magenta annuli in Figure 3). We also show the results of different radial binning of three annuli (dashed line). Black solid line is the best-fit temperature profile. We added the hardness ratio profile in the top panel (green open circles). Magenta (green) solid line is the average metal abundance profile of CC (NCC) clusters studied in Ettori et al. (2015).

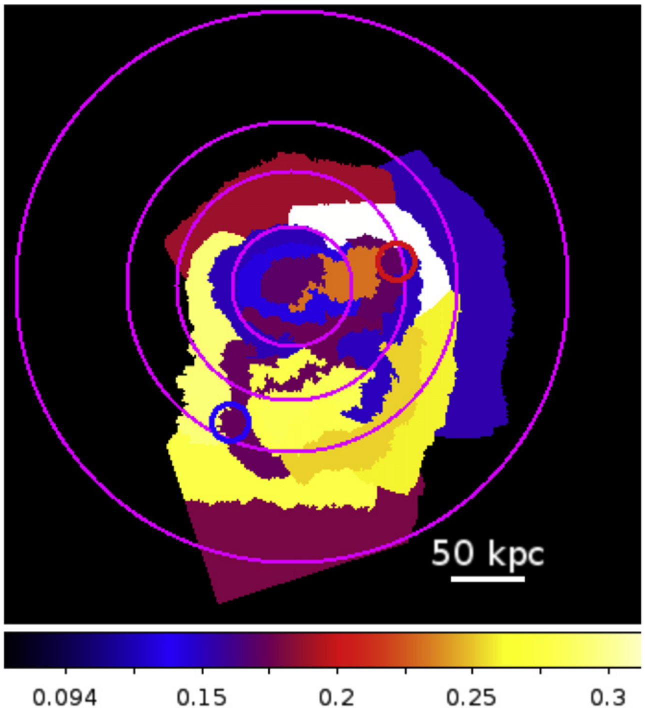

Figure 3. Contour binning hardness ratio map of Abell 1142 (2.0–7.0 keV to 0.5–2.0 keV). Blue and red circles indicate the locations of two BCGs. Magenta annuli, centered on the peak of X-ray emission, represent extraction regions of spectral analysis (Figure 2).

target field. A few rounds of self-calibration were carried out to refine the gain solution of the target field. The data were then combined and jointly deconvolved to produce the final primary beam-corrected image of the cluster. Clean boxes were used during the imaging as was W-projection (Cornwell et al. 2008). We used Briggs et al. (1995) weighting with a robust factor of −0.5, resulting in an image with a resolution of $8''.0 \times 7''.4$. At the cluster position, we measure an rms noise of 0.37 mJy beam^{-1}.

The integrated 1.4 GHz flux density for the source from the NVSS (Condon et al. 1998), which should recover all of the flux, is 42.5 ± 1.3 mJy. This corresponds to a 1.4 GHz radio power of 1.2×10^{23} W Hz^{-1}.

3. RESULTS

3.1. *Thermal and Chemical Distribution*

Despite the overall asymmetric morphology of the X-ray emission, we generated the azimuthally averaged surface brightness profile centered on the central X-ray peak as shown in Figure 4. Black (red) circles were produced with the central 20 kpc emissions from Peaks G1 and G2 excluded (included). Emissions from Peaks G1 and G2 are likely to be dominated by the ISM of the BCGs. The surface brightness profile with G1 and G2 excluded provides a better trace of the smooth ICM distribution. We fit the profile of black circles to a single β model:

$$S(r) = S_0\left[1 + \left(\frac{r}{r_c}\right)^2\right]^{-3\beta+1/2}.$$

We obtained best-fitting parameter values of $\beta = 0.45 \pm 0.04$ and $r_c = 92 \pm 16$ kpc with a χ^2/ndf of 132/47. The fit was significantly improved by applying a double β model instead (here we linked the values of the two β):

$$S(r) = S_{01}\left[1 + \left(\frac{r}{r_{c1}}\right)^2\right]^{-3\beta+1/2} + S_{02}\left[1 + \left(\frac{r}{r_{c2}}\right)^2\right]^{-3\beta+1/2}.$$

We obtained best fits of $\beta = 0.65 \pm 0.13$ and $r_{c1}(r_{c2}) = 12 \pm 4\ (157 \pm 31)$ kpc with a χ^2/ndf of 106/45.

Vikhlinin et al. (2006) presented a universal profile to model the temperature profiles of cool-core clusters:

$$T_{3D}(r) = \frac{[T_0(r/r_{\rm cool})^{a_{\rm cool}} + T_{\rm min}]}{[(r/r_{\rm cool})^{a_{\rm cool}} + 1]} \times \frac{(r/r_t)^{-a}}{[1 + (r/r_t)^b]^{c/b}}. \quad (1)$$

We fit the projected temperature profile of Abell 1142 to this universal profile and obtained a best fit of $[T_0, r_{\rm cool}, a_{\rm cool}, T_{\rm min}, r_t, a, b, c] = [3.93, 23.9, 3.13, 0.044, 380.7, 0.012, 1.36, 2.24]$ as shown in Figure 2. These parameters are poorly constrained.

Abell 1142 resembles a scaled-down version of the Coma Cluster, which is a massive NCC cluster containing two dominant early-type galaxies (NGC 4874 and NGC 4889) with the cluster X-ray emission peak residing between them. However, unlike the Coma Cluster, the X-ray peak of Abell 1142 is substantially cooler than its surroundings, as presented in Figures 2 and 3. We observe a temperature below 2.0 keV toward the center which rises to 3.5 keV just outside 50 kpc, then declines to 2.5 keV out to 200 kpc. In addition, its metal abundance profile reaches 0.7 $Z_\odot$ at the center and gradually declines to ~0.1 $Z_\odot$ out to 200 kpc. The behaviors of the temperature and metal abundance profiles are very typical of those observed in CC clusters (De Grandi & Molendi 2001; Maughan et al. 2012). We also fit the spectrum extracted from

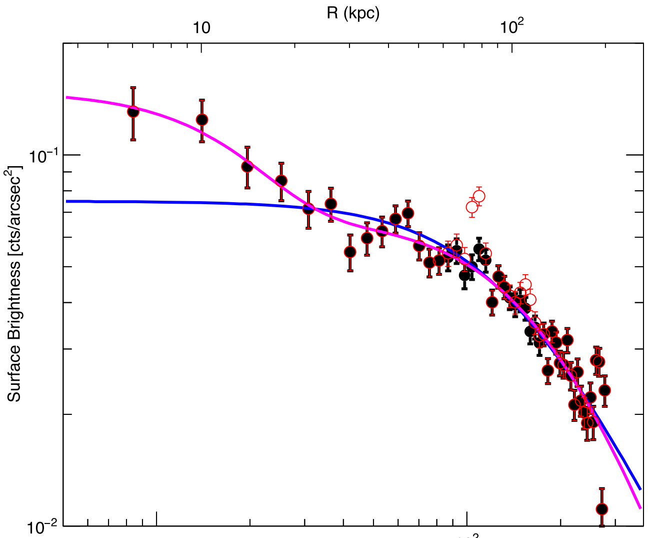

Figure 4. Surface brightness profile of Abell 1142 in the energy band 0.5–4.0 keV, centered on the cluster X-ray emission peak (cyan cross in Figure 1). Blue solid line indicates the best-fit single β model with $\beta = 0.45 \pm 0.04$ and $r_c = 92 \pm 16$ kpc. Magenta solid line indicates the best-fit double β model with $\beta = 0.65 \pm 0.13$ ($r_{c1} = 12 \pm 4$ kpc and $r_{c2} = 157 \pm 31$ kpc).

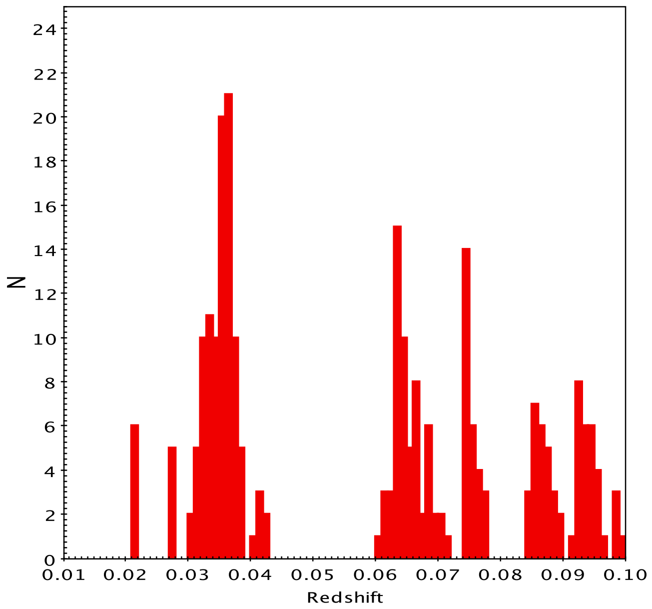

Figure 5. Histogram of all the available redshifts in the SDSS database and NED within a 60′ field (galaxies with $z > 0.1$ are not shown for display purposes). The Abell 1142 cluster stands out as the redshift peak at $z = 0.035$.

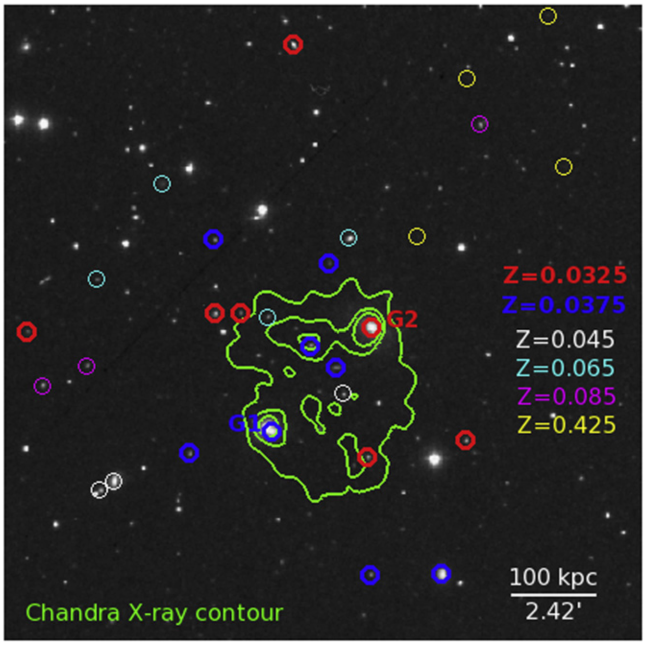

Figure 6. DSS image galaxies of the central 18′ × 18′ of Abell 1142. *Chandra* X-ray contour is based on a adaptively smoothed image; contour levels are at $[0.9, 1.5, 2.1] \times 10^{-9}$ photon cm^{-2} s^{-1}. We overlaid the redshift distributions of SDSS galaxies (only those with at least three galaxies per redshift bin are shown here).

the central 20″ but fixed its metallicity at the current best-fit value of the central 65″, and obtained a best-fit temperature of $1.92^{+0.36}_{-0.31}$ keV and an electron density n_e of $5.8 \pm 0.3 \times 10^{-3}$ cm^{-3}, where n_e is calculated through

$$\text{norm} = \frac{10^{-14}}{4\pi[D_A(1+z)]^2}\int n_e n_H dV.$$

3.2. Galaxies in Abell 1142

We selected all of the galaxies with known recession velocities from NED and SDSS within 60′ (2.4 Mpc at the redshift of the source). The SDSS data are augmented by the redshift surveys of the object performed by Geller et al. (1984), Mahdavi & Geller (2004), and Quintana & Ramirez (1995). Group members have been selected through the elimination of background and foreground galaxies along the line of sight to Abell 1142. As a first step, we applied the “velocity gap” method (De-Propris et al. 2002) sorting the galaxies in redshift space and calculating their velocity gap, defined for the nth galaxy as $\Delta v_n = cz_{n+1} - cz_n$. We use 1000 km s^{-1} as the velocity gap. Figure 5 shows that Abell 1142 is clearly detected as a peak at $z = 0.03 - 0.04$ populated by 102 candidate member galaxies. In Figure 6, we marked out the locations of galaxies with accurate SDSS redshifts on the DSS optical image in the central 18′ × 18′. The distribution of galaxies in the range $z = 0.03 - 0.04$ overlaps with the X-ray emission contour of the *Chandra* observation of Abell 1142. In contrast, the distribution of galaxies in other redshift bins appears to be offset from the X-ray emission in projection. The X-ray emission, in particular, the emission peak, is unlikely to be a background cluster.

As a second step, we used the “shifting gapper” method (Fadda et al. 1996). In this method, interlopers are separated from members by exploiting both radial and peculiar velocity information. The data are binned radially such that each bin contains at least 20 objects. The peculiar velocities of the galaxies are calculated as $v_{\rm pec} = c((1 + z_{\rm pec})^2 - 1)/((1 + z_{\rm pec})^2 + 1)$, where c is the speed of light, $z_{\rm pec} = (z_{\rm gal} - z_{\rm cos})/(1 + z_{\rm cos})$ is the peculiar redshift of the galaxy, and $z_{\rm cos}$ is the mean group velocity estimated by the biweight location estimator (Beers et al. 1990) and is assumed to represent the cosmological redshift of the group. Within each bin galaxies are sorted by peculiar velocity with velocity gaps determined in peculiar velocity. Galaxies are rejected as interlopers if their peculiar velocity gaps are above the value of the “f pseudosigma” (Beers et al. 1990), an estimator robust

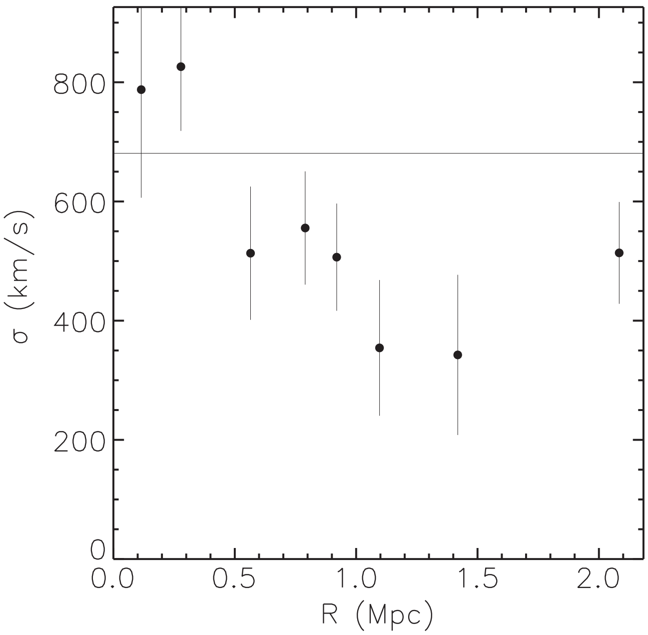

Figure 7. Velocity dispersion profile of the Abell 1142 cluster where the center of the group is assumed to be at the position of the galaxy IC 664. Bins contain 10 galaxies each and 1σ jackknife errors are shown. The solid line shows the expected value of dispersion velocity assuming density-energy equipartition between IGM and galaxies, i.e., $\beta_{\rm spec} = 1$.

to the presence of outliers. The above procedure was iterated until the number of members was stable.

The shifting gapper is able to exclude a group of high-velocity galaxies ($cz_{\rm gal} > 12{,}500\ {\rm km\ s^{-1}}$) and a group of low-velocity galaxies ($cz_{\rm gal} < 9500\ {\rm km\ s^{-1}}$) already discussed by Geller et al. (1984) as interlopers associated with the nearby galaxy cluster Z1056.9+0922. The final group sample contains 88 members. The value for the biweight location estimator of the mean group velocity is $10614 \pm 73\ {\rm km\ s^{-1}}$, which corresponds to $z_{\rm cos} = 0.0354 \pm 0.0002$. We used the biweight scale estimator to estimate a velocity dispersion of $575 \pm 36\ {\rm km\ s^{-1}}$. The errors for the redshift and velocity dispersion are 1σ and are estimated using the jackknife resampling technique.

In Figure 7, we show the velocity dispersion profile derived for the data. Bins contain 10 galaxies each and velocity dispersions have been calculated using the gapper algorithm (Beers et al. 1990). The velocity dispersion profile shows some interesting features: it flattens at high radii, possibly due to a robust asymptotic value in the external group regions, as found for the majority of nearby clusters (e.g., Fadda et al. 1996, Girardi et al. 1996). The increase at radii larger than 2 Mpc indicates likely interloper contamination. Furthermore, the relation used to calculate $R_{200} = \sqrt{3}\,\sigma/10H(z)$ (Carlberg et al. 1997)[4] gives a value of 1.4 Mpc. We therefore restrict the member galaxies to the 67 ones within 1.5 Mpc. Their redshift distribution shows a bimodal distribution as shown in Figure 8. We fit this histogram to a model consisting of two Gaussian distributions. Each distribution peaks at $z = 0.033$ and $z = 0.037$, respectively. This corresponds to a $1200\ {\rm km\ s^{-1}}$ rest-frame velocity difference with velocity dispersions of 175 and $360\ {\rm km\ s^{-1}}$. We marked these two populations in blue and red, respectively, in Figure 6. They overlap in projection with G1 and G2 each belonging to one population. The radial velocity difference between G1 ($z_{\rm G1} = 0.0373$) and G2 ($z_{\rm G2} = 0.0338$) is only $1000\ {\rm km\ s^{-1}}$.

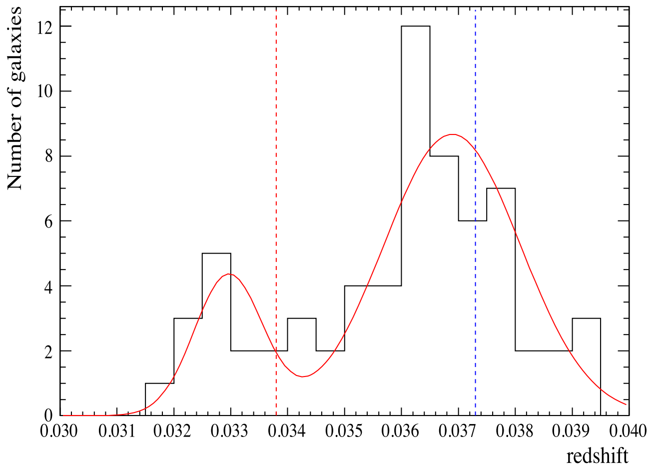

Figure 8. Histogram of the redshifts of the final sample of members of A1142 within 1.5 Mpc using a bin size of $\Delta z = 0.0005$. Blue and red dashed lines indicate the redshifts of G1 and G2, respectively.

We can therefore conclude that there is evidence for a merger in Abell 1142. In particular, the high dispersion velocity in the core ($\sim 800\ {\rm km\ s^{-1}}$) is indicative of the presence of substructures. We speculate that a subgroup comprising G2 is merging with the main body of Abell 1142 to which G1 belongs. A likely lower limit on the velocity of the merger can be estimated by the line-of-sight difference of velocities between the mean of the components of G1 and G2, and therefore is $1000\ {\rm km\ s^{-1}}$. This merger is mostly at the cluster center while the larger radii of the cluster are relatively relaxed.

3.3. The BCGs

We note that G1 is made up of three individual galaxies, instead of a single galaxy, as shown in the SDSS *R*-band image in Figure 6, labeled as Objects 1, 2, and 3 (Object 0 is a foreground star). All of them appear to be elliptical galaxies. SDSS measured a spectroscopic redshift for Object 1 of $z = 0.03729$, consistent with the average of "the G1 sub-cluster." The spectroscopic redshifts of Objects 2 and 3 cannot be obtained through SDSS since they are separated by $\lesssim 3''$ from each other, falling short of the fiber size of SDSS. The redshifts of Objects 2 and 3 found in the literature are similar to Object 1 but their values and positions are inconsistent. Reliable redshift measurements are currently unavailable, although they seem unlikely to be background objects.

We also show the *Chandra* X-ray image, VLA radio image, and 2MASS *K*-band images of the same field of view in Figure 9. Objects 1 and 2 contain X-ray nuclei detected by `wavedetect`. We inspected the 2.0–8.0 keV image and confirmed that they are point sources. They also contain point sources in the radio band. Objects 1 and 2 may each harbor an AGN. We obtained count rates from the point source regions given by `wavedetect`. We derived X-ray luminosities of $1.6 \pm 0.7 \times 10^{40}\ {\rm erg\ s^{-1}}$ and $6.3 \pm 1.1 \times 10^{40}\ {\rm erg\ s^{-1}}$ in the 2–8 keV band for the AGNs in Objects 1 and 2, respectively, assuming a power-law spectrum with an index of 1.4. All three of these galaxies appear to have similar *R*-band and *K*-band luminosities. They may have similar stellar masses.

---

[4] The radius within which the enclosed average density is 200 times the critical density of the Universe.

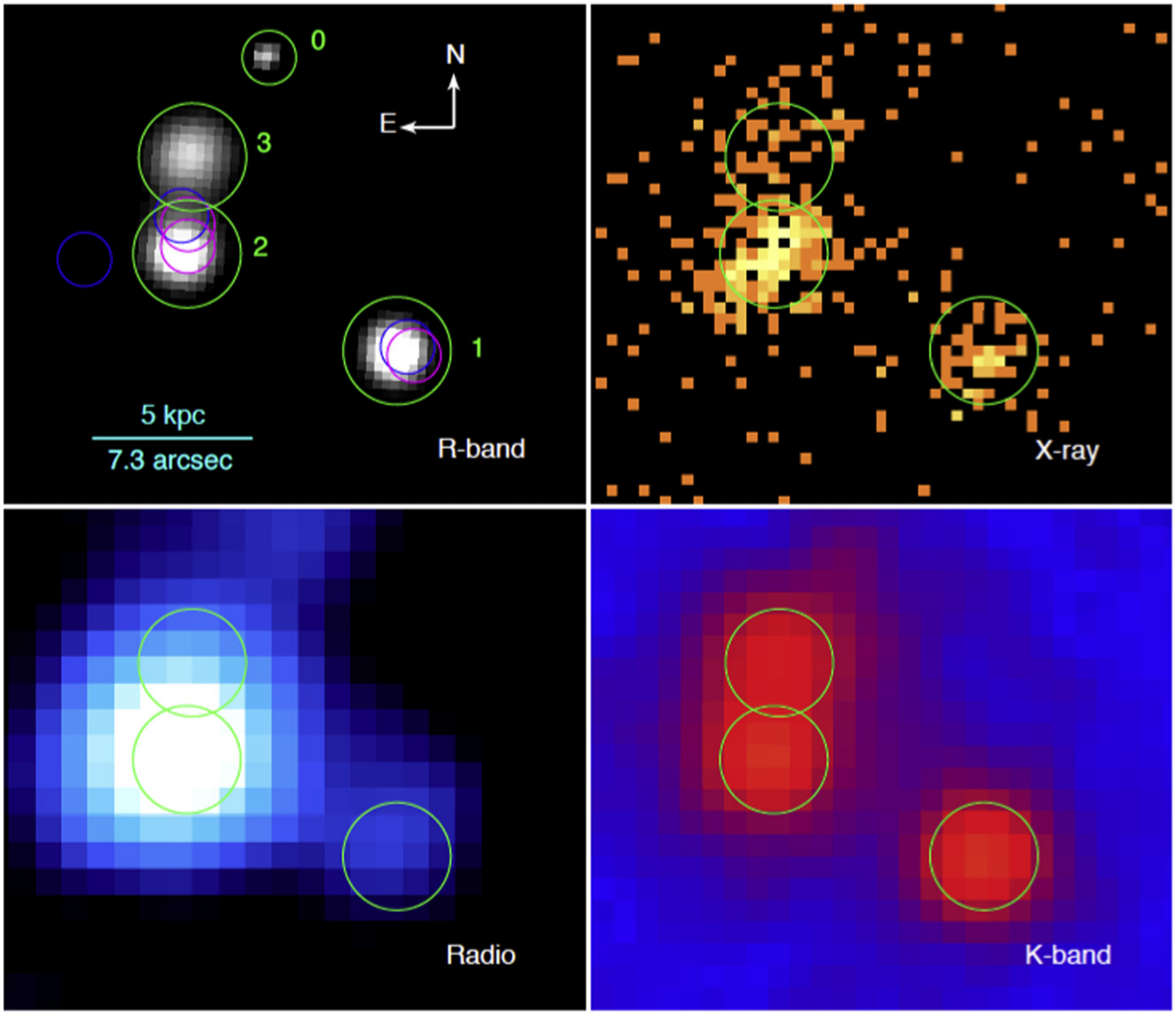

Figure 9. *R*-band (SDSS), X-ray (*Chandra*), Radio (VLA), and *K*-band (2MASS) images of G1 (NGC 3492) on the same scale. Objects 1, 2, and 3 are early-type galaxies. Object 0 is a foreground star. Magenta circles are positions of three galaxies listed in NED and blue circles are three galaxies listed in HyperLeda.

Member galaxies orbiting in the ICM would gradually lose angular momentum to the background ICM, stars, or dark matter through dynamical friction. This effect becomes progressively significant toward the cluster center (El-Zant et al. 2004; Gu et al. 2013). Given their current positions (possibly within a radius of 5 kpc), these three galaxies are anticipated to sink into the center of the G1 subcluster within a time much shorter than the infall time in a cuspy dark matter halo (Cole et al. 2012). While the projected distances of the galaxies in question are currently unknown, if they all lie within ~5kpc of the BCG, then it would have important consequences for the shape of the dark matter profile. The four galaxies found in the 10 kpc core of Abell 3287 are another example (Massey et al. 2015).

We derived the *K*-band infrared luminosities of G1 and G2 using 2MASS archived images (Skrutskie et al. 2006). We obtained an average $L_{\rm K,G1} = 2 \times 10^{11} L_{\rm K,\odot}$ for each contained in G1 (one-third of the total *K*-band luminosity of G1) and obtained $L_{\rm K,G2} = 2.66 \times 10^{11} L_{\rm K,\odot}$ for G2, IC 664.

We were unable to perform X-ray spectral analysis of the faint ISM of G1 or G2 due to the limited exposure. Based on their net count rates, we estimated gaseous X-ray luminosities within two effective radii of G1 and G2 using PIMMS, assuming an ISM temperature of 0.5 keV and a metal abundance of 0.7 $Z_\odot$ (typical of early-type galaxies, Su & Irwin 2013; Su et al. 2015b). We excluded contributions from low-mass X-ray binaries and stellar diffuse emission based on their *K*-band luminosities.[5] This leads to gaseous X-ray luminosity to *K*-band luminosity ratios of 5×10^{28} erg s^{-1} $L_{\rm K\odot}{}^{-1}$ and 7×10^{29} erg s^{-1} $L_{\rm K\odot}{}^{-1}$ for G1 and G2, respectively. (We assume that all three G1 galaxies have the same diffuse X-ray luminosities.) We compare G1 and G2 with other early-type galaxies studied in Su et al. (2015b) in Figure 11. Group center galaxies are marked in black solid circles. The $L_{\rm X,gas}/L_{\rm K}$ of G1 and G2 are typical of group center galaxies. This result reinforces the status of G1 and G2 as BCGs.

---

[5] For stellar diffuse emission (cataclysmic variables and active binaries), we use the relation calibrated by Revnivtsev et al. (2008): $L_{\rm X_{CV/AB}}/L_{\rm K} = 5.9 \times 10^{27}$ erg s^{-1} $L_{\rm K\odot}{}^{-1}$. For low-mass X-ray binaries, we use the relation calibrated by Boroson et al. (2011): $L_{\rm X_{LMXB}}/L_{\rm K} = 10^{29}$ erg s^{-1} $L_{\rm K\odot}{}^{-1}$.

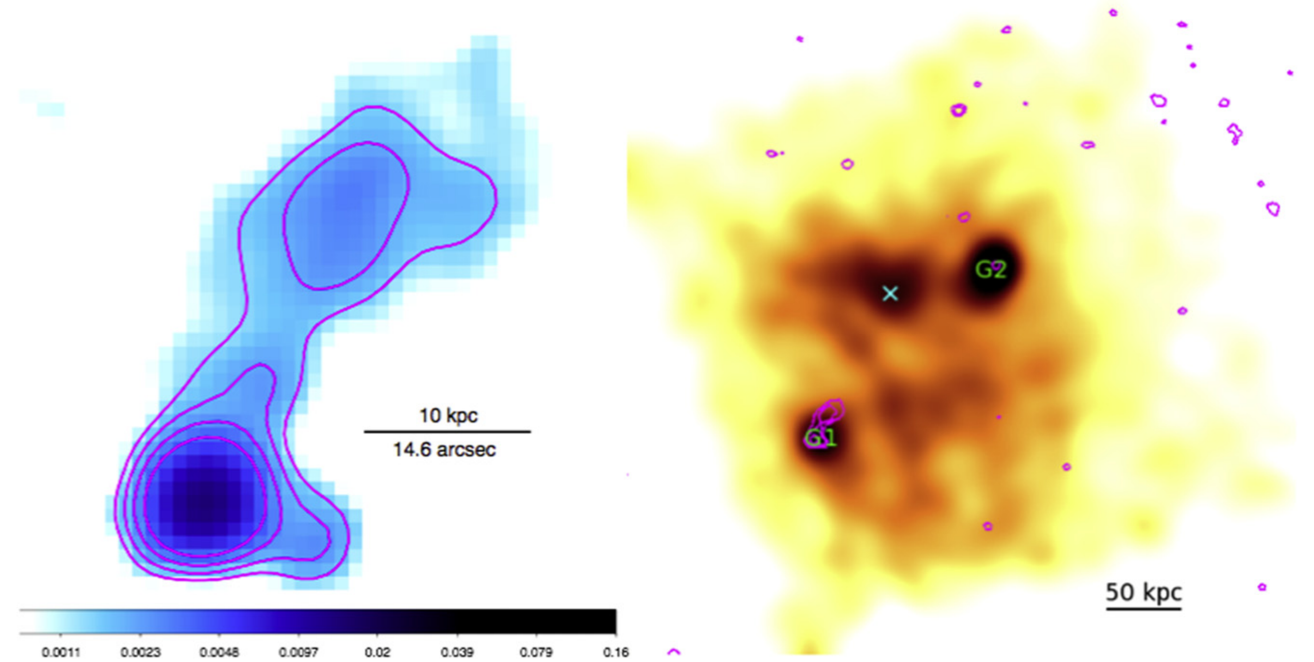

Figure 10. Left: VLA radio image of G1 showing extended radio emission in the northwest direction in units of Jy beam^{-1}. Magenta contour levels are set at sqrt[1, 2, 4, 8] × $4\sigma_{\mathrm{rms}}$, where $\sigma_{\mathrm{rms}} = 0.37$ mJy beam^{-1}. Right: *Chandra* X-ray image of Abell 1142 with the radio contour overlaid.

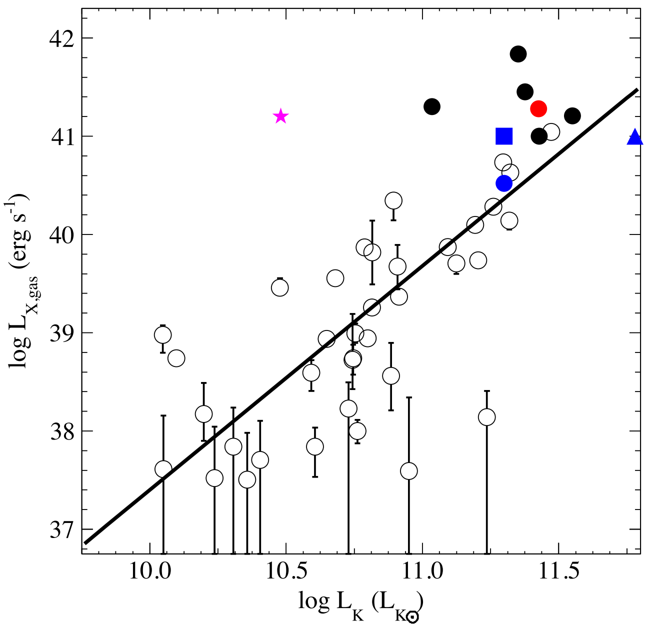

Figure 11. Gaseous X-ray luminosities as a function of *K*-band luminosities for all galaxies taken from Su et al. (2015b). The black solid line is the best-fit $L_{X_{\mathrm{gas}}}$–L_K relation. Black solid circles indicate group center galaxies. Red circle represents IC 664 (G2). Blue symbols represent NGC 3492 (G1)–blue circle: using the average $L_{X_{\mathrm{gas}}}$ and L_K of the three galaxies in G1; blue square: assuming all the $L_{X_{\mathrm{gas}}}$ is from one of the three galaxies; blue triangle: treating all three galaxies as one galaxy (total $L_{X_{\mathrm{gas}}}$ and L_K). Magenta star represents the small galaxy at the central X-ray peak.

The VLA image of G1 reveals that it contains a radio tail pointing northwest, approximately 10 kpc wide and 30 kpc long (Figure 10). It appears to be more extended than other background radio sources found in the same VLA observation. It may be a radio lobe ejected by Object 2. The direction of this tail suggests that G1 may move southeastward in the plane of the sky. We note that while G1 harbors a radio lobe, G2 only contains a small radio point source. This is consistent with our speculation that G2 is the center of a subcluster merging with the main body of Abell 1142 centered at G1.

We note that there is a galaxy located right at Peak X with nearly the same redshift as G1 (Figure 6). Its *K*-band luminosity is only $3 \times 10^{10} L_{K\odot}$, i.e., 10 times smaller than G1 and G2. Its associated X-ray emission is very unlikely to be dominated by the ISM of this relatively small galaxy. First, the temperature of the gas inferred in the smallest aperture is close to 2 keV, which implies a group-scale, rather than a galaxy-scale, halo. Second, the $L_{X,\mathrm{gas}}/L_K$ ratio would place this object far off the relation in Figure 11 (magenta star). For these reasons, it is most likely that the X-ray peak is dominated by cluster emission.

4. DISCUSSION

Abell 1142 is a unique object invoking some important implications discussed in the following subsections.

4.1. Is Abell 1142 a Cool-core Cluster?

Several pieces of evidence suggest that Abell 1142 is a CC cluster: the positive temperature gradient, the negative metal abundance gradient, and the need for a double β model, although its morphology and the offset between its X-ray emission peak and BCG are not as typical of CC clusters.

Quantitatively distinguishing CC and NCC clusters is more problematic than it might seem at first because even classic morphologically disturbed NCC clusters like Coma can possess isolated regions of temperature drops. Here, we consider two criteria that have been proposed to distinguish a CC from an NCC cluster. One criteria is that the ICM cooling time at the center of the CC (NCC) clusters should be shorter (longer) than the look back time to $z = 1$ (i.e., 7.7 Gyr; Birzan et al. 2004; Hudson et al. 2010). The other criteria is that CC (NCC) clusters should have a central entropy smaller (larger) than 70 keV cm^2 (Mahdavi et al. 2013). Using the best-fit electron density and temperature determined for the central 20″ (14 kpc), we calculate the cooling time profile from Voigt & Fabian (2004) as

$$t_{\rm cool} = 20\left(\frac{n_e}{10^{-3}\,{\rm cm}^{-3}}\right)^{-1}\left(\frac{T}{10^7\,{\rm K}}\right)^{0.5}{\rm Gyr}$$

and the entropy profile as $S = kT/n_e^{2/3}$. We obtained $t_{\rm cool} = 5.1^{+0.8}_{-0.7}$ Gyr and $S = 59.6^{+13.7}_{-11.3}$ keV cm^2, which marginally satisfy the CC criterion.

The difference between CC and NCC clusters is not only in thermo-dynamics but also in chemo-dynamics. The central gas in CC clusters is more metal rich than NCC systems. Using *XMM-Newton*, Ettori et al. (2015) studied the metal abundance distribution of 83 clusters out to a radius of $>0.4\,R_{500}$. Their work provided a representative radial and redshift dependence in the form of $Z(r, z) = Z_0(1 + (r/0.15R_{500})^2)^{-\beta}(1 + z)^{-\gamma}$, with $(Z_0, \beta, \gamma) = (0.83 \pm 0.13, 0.55 \pm 0.07, 1.7 \pm 0.6)$ for CC clusters and $(Z_0, \beta, \gamma) = (0.39 \pm 0.04, 0.37 \pm 0.15, 0.5 \pm 0.5)$ for NCC clusters. We compared the metal abundance profile of Abell 1142 to these average profiles of CC and NCC clusters in Figure 2 (bottom). The central metallicity of Abell 1142 is very typical of CC clusters.

Overall, the current results suggest that it is entirely possible for Abell 1142 to harbor a cool core at its center although it is not very pronounced. Note that these values are very uncertain. Our use of projected profiles to derive these parameters may also smear out "cool-core" features. In addition, these standards are very arbitrary and may not apply well to a lower-temperature and asymmetric system like Abell 1142. On the other hand, if the temperature of the surrounding hot gas was greatly enhanced due to shock heating, the relative significance of this "cool core" would be undermined.

4.2. Ongoing Merging Scenario

We estimate a velocity dispersion for Abell 1142 of 575 km s^{-1}. This corresponds to a thermal temperature of 2.6 based on the σ–T_X relation calibrated by Wu et al. (1999) for galaxy clusters. Bohringer et al. (2000) listed a *ROSAT* X-ray luminosity of $L_X = 2.8 \times 10^{43}$ erg s^{-1} in 0.1–2.4 keV for Abell 1142, which translates to a T_X of 1.4 keV based on the L_X–T_X relation of Wu et al. (1999). Note that there are large internal scatters of the σ–T_X and L_X–T_X relations as well. Nevertheless, the fact is that we observe $T_X = 3.5$ keV for Abell 1142, which is higher than we expect and could be a sign of recent shock heating caused by a merger.

Abell 1142 may contain two subclusters, likely with G1 and G2 being their BCGs. These two subclusters may be experiencing merging with a velocity difference of 1000 km s^{-1} in the line of sight. The thermal temperature (preshock temperature) of Abell 1142 should be in the range of 1.4–2.6 keV. The fact that we observe ~3.5 keV hot gas indicates the effect of shock heating caused by this merger. The temperature jump is directly related to the Mach number through the Rankine–Hugeniot equation:

$$\frac{T_2}{T_1} = \left[\frac{2\gamma\mathcal{M}^2 - (\gamma - 1)}{(\gamma + 1)^2}\right]\left[\gamma - 1 + \frac{2}{\mathcal{M}^2}\right].$$

The Mach number is expected to be the ratio of the merging velocity to the sound speed ($\mathcal{M} = v/c_s$), and the sound speed in the plasma can be expressed as a function of the preshock temperature (T_1) as $c_s = \sqrt{(\gamma kT_1)/(\mu m_{\rm H})}$, where $\gamma = 5/3$ and $\mu = 0.62$. These connections allow us to express the merging velocity as a function of the preshock temperature for Abell 1142 as shown in Figure 12. The green solid line represents a postshock temperature (T_2) of 3.5 keV (Figure 2), which is a projected temperature. The actual postshock temperature is more likely to be 4.0 keV (or even 4.5 keV), marked as a magenta line. The actual scenario could be anywhere between a 1100 km s^{-1} merger in an originally 2.6 keV ICM and a 1550 km s^{-1} merger in an originally 1.4 keV ICM. Even these upper and lower limits are not hard limits since these values are just rough estimates. Considering that the ICM temperature of Abell 1142 drops to 2.5 keV out to 200 kpc (Figure 2), we use 2.5 keV as the preshock temperature of the ICM. This corresponds to a merging velocity of 1200 km s^{-1} between the two subclusters.

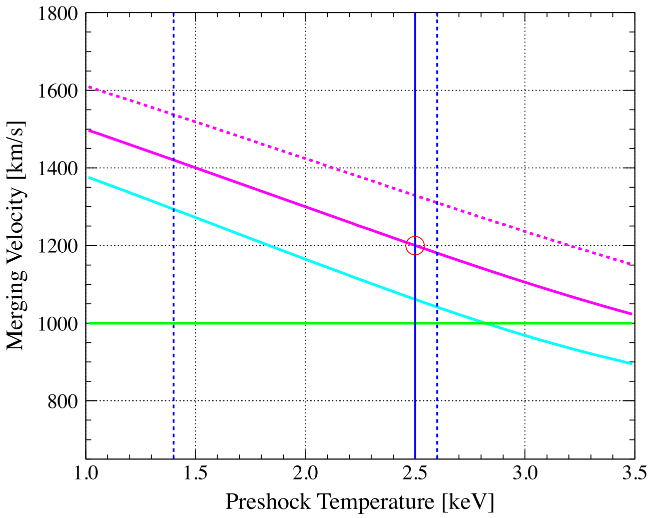

Figure 12. Estimated merging velocities between the two subclusters as a function of the ICM preshock temperatures for Abell 1142. Cyan and magenta solid (dashed) lines represent postshock temperatures of 3.5 and 4.0 keV (4.5 keV), respectively. Green solid lines indicate 1000 km s^{-1}, the radial merging velocities inferred from the redshift distributions of member galaxies. Two blue dashed lines indicate 1.4 and 2.6 keV, covering the range of preshock temperatures inferred from the cluster L_X and σ, respectively. We marked a preshock temperature of 2.5 keV with the blue line, inferred from the temperature profile of Abell 1142 out to 200 kpc. Red circle indicates the most likely scenario.

The cool core at the center of Abell 1142 could be a remnant of either G1 or G2 as the merger displaced this cool core from its BCG. Supposedly, the total velocity difference is 1200 km s^{-1} with a line-of-sight velocity difference of 1000 km s^{-1}. This corresponds to a velocity difference of 660 km s^{-1} in the plane of the sky between G1 and G2 (with G1 moving eastward and G2 moving westward). G1 or G2 may move at a transverse velocity of 330 km s^{-1} relative to the rest frame. It is unclear whether this "cool core" used to belong to G1 or G2. In projection, it overlaps with member galaxies in the G1 subcluster and the radio tail of G1 points directly to this cool core. However, it is more connected to G2 than G1 through X-ray emission and it is more likely for the less massive subcluster to have had its cool core displaced in a merger. In either case, the current "cool core" is 100 kpc away from its BCG in projection. The separation between the cool core and its BCG may have occurred 100 Myr ago.

4.3. Chemical Enrichment Processes

The spectral analysis of Abell 1142 shows that its ICM has a metal abundance peak of ~0.7 $Z_\odot$ at the cluster center, which is cooler than the ambient ICM. The origin of the metals at the cluster center should be directly related to the formation of this cool region lacking a BCG. At least two pictures start to emerge: (1) this cool region was formed through the accumulation of cold gas stripped from infalling subgroups/galaxies during their passages of the cluster center, or (2) the major merger left a cool core (as in the cool-core remnant scenario, Rossetti & Molendi 2010) that was stripped from its BCG. In the first scenario, the source of the metal is supplied by the newly accreted/formed subgroups/galaxies; such metals should be rich in SN II production. In the second scenario, the source of the metal is the ejection from the BCG before the cool core was separated from its BCG; such metals should be rich in SN Ia production. Indeed, this metal-rich, cool region could be the ISM stripped from either G1 or G2 rather than being a cool-core remnant. Typical examples include the ram pressure stripped galaxy M86 falling through the Virgo Cluster (Randall et al. 2008), the stripped subcluster as a result of the off-axis merger in RXJ0751+5012 (Russell et al. 2014), and the prominent stripped tail in the outskirt of Abell 2142 (Eckert et al. 2014). Then again, unlike these typical stripped tails, the cool region in Abell 1142 is not in a tail-like shape and it lacks an uninterrupted bridge of emission from the main body. Deeper exposure of Abell 1142 would allow us to determine the metal content of elements other than Fe (e.g., α-elements) with which we can unveil the enrichment process of Abell 1142 and cast light on the formation of this cool region.

The metal abundance profile of Abell 1142 gradually declines to ~0.1 $Z_\odot$ out to 200 kpc. This could be a result of the "Fe-bias" caused by multi-temperature gas (Buote 2000), and its metallicity could still be as high as ~0.3 $Z_\odot$ due to the large uncertainty. Nevertheless, a possible low abundance in the ICM outside the cluster core would suggest a lack of early enrichment in poor clusters. This would provide a sharp contrast to massive CC clusters like the Perseus Cluster with its ICM uniformly enriched (~0.3 $Z_\odot$) out to the virial radius (Werner et al. 2013). Nevertheless, this may support infalling galaxies and subgroups in poor clusters posibly being able to retain their enriched gas until they reach the denser cluster core (Su et al. 2014; Elkholy et al. 2015).

5. CONCLUSIONS

We present a *Chandra* observation of Abell 1142, a poor cluster containing two BCGs (G1 and G2). Its central X-ray emission peak is offset from both BCGs by ~100 kpc. This peak corresponds to a cool and metal-enriched region compared with the surrounding cluster gas. The azimuthally averaged surface brightness profile centered on this X-ray peak can be well described by a double β model. These features are very suggestive of a cluster cool core. The redshift distribution of its member galaxies indicates that Abell 1142 may consist of two subclusters that are merging at a relative velocity of $\approx$1000 km s^{-1} in the line of sight. G1 belongs to the more massive subcluster while G2 belongs to the less massive subcluster. Its ICM temperature may be elevated due to shock heating.

Perhaps one of the subclusters used to be a typical, relaxed CC cluster. This merger caused its metal-enriched cool core to be displaced from its BCG. We may witness the onset of a CC cluster being transformed into an NCC cluster through major mergers. In an alternative scenario, this metal-rich, cool region is formed through the accumulation/stripping of cold gas supplied by infalling subgroups/galaxies.

We note that G1 is made up of three individual galaxies residing within a radius of 5 kpc in projection. Either the dynamical friction is smaller than expected from a cuspy dark matter halo, or we happened to capture these galaxies as they are merging before they sink into the cluster center.

We are thankful for helpful discussions with William Forman, Manoj Kaplinghat, Tiziana Venturi, and Ralph Kraft. D.A.B. and Y.S. gratefully acknowledge partial support from the National Aeronautics and Space Administration under grant No. NNX13AF14G issued through the Astrophysics Data Analysis Program. Partial support for this work was also provided by NASA through *Chandra* Award No. GO2-13159X issued by the *Chandra* X-ray Observatory Center, which is operated by the Smithsonian Astrophysical Observatory for and on behalf of NASA under contract NAS8-03060. This publication makes use of data products from the Two Micron All-Sky Survey, which is a joint project of the University of Massachusetts and the Infrared Processing and Analysis Center/California Institute of Technology, funded by the National Aeronautics and Space Administration and the National Science Foundation. Funding for the SDSS and SDSS-II has been provided by the Alfred P. Sloan Foundation, the Participating Institutions, the National Science Foundation, the U.S. Department of Energy, the National Aeronautics and Space Administration, the Japanese Monbukagakusho, the Max Planck Society, and the Higher Education Funding Council for England. The SDSS Web Site is http://www.sdss.org/. The SDSS is managed by the Astrophysical Research Consortium for the Participating Institutions. This paper is dedicated to the loving memory of Y. S.'s late grandfather Hua Li.

REFERENCES

Abdullah, M., Ali, G., Ismali, H., et al. 2011, MNRAS, 416, 2027
Balucinska-Church, M., & McCammon, D. 1992, ApJ, 400, 699
Beers, T. C., Flynn, K., & Gebhardt, K. 1990, AJ, 100, 32
Birzan, L., Rafferty, D. A., McNamara, B. R., et al. 2004, ApJ, 607, 800
Bohringer, H., Voges, W., Huchra, J. P., et al. 2000, ApJS, 129, 435
Bohringer, H., & Werner, N. 2010, A&AR, 18, 127
Boroson, B., Kim, D., & Fabbiano, G. 2011, ApJ, 729, 12
Briggs, D. S. 1995, Ph.D. Thesis, New Mexico Inst. of Mining & Technology
Buote, D., & Tsai, J. 1996, ApJ, 458, 27
Buote, D. 2000, MNRAS, 311, 176
Buote, D. 2001, in Astrophysics and Space Science Library, 272, Merging Processes in Galaxy Clusters, ed. L. Feretti, I. M. Gioia, & G. Giovannini (Dordrecht: Kluwer), 79
Buote, D. 2001, ApJ, 539, 172
Buote, D., Lewis, A. D., Brighenti, F., et al. 2003, ApJ, 595, 151
Burns, J., Hallman, E., Gantner, B., et al. 2008, ApJ, 675, 1125
Carlberg, R. G., Yee, H. K. C., & Ellingson, E. 1997, ApJ, 478, 462
Cavagnolo, K., Donahue, M., Voit, M., et al. 2009, ApJS, 182, 12
Cole, D. R., Dehnen, W., Read, J. I., et al. 2012, MNRAS, 426, 601
Condon, J. J., Cotton, W. D., Greisen, E. W., et al. 1998, AJ, 115, 1693
Cora 2006, MNRAS, 386, 1540
Cornwell, T. J., Golap, K., & Bhatnagar, S. 2008, ISTSP, 2, 647
De Grandi, & Molendi 2001, ApJ, 551, 153

De Luca, A., & Molendi, S. 2004, A&A, 419, 837
De Propris, R., Couch, W. J., & Colless, M. 2002, MNRAS, 329, 87
Dickey, J. M., & Lockman, F. J. 1990, ARA&A, 28, 215
Eckert, D., Molendi, S., Owers, M., et al. 2014, A&A, 570, 119
Elkholy, T. Y., Bautz, M. W., & Canizares, C. R. 2015, ApJ, 805, 3
El-Zant, A., Kim, W., & Kamionkowski, M. 2004, MNRAS, 354, 169
Ettori, S., Baldi, A., Balestra, I., et al. 2015, A&A, 578A, 46
Fabian, A. 2012, ARA&A, 50, 455
Fadda, D., Girardi, M., Giuricin, G., et al. 1996, ApJ, 473, 670
Finoguenov, A., David, L. P., & Ponman, T. J. 2000, ApJ, 544, 188
Geller, M. J., Beers, T. C., Bothun, G. D., et al. 1984, AJ, 89, 319
Girardi, M., Fadda, D., Giuricin, G., et al. 1996, ApJ, 457, 61
Gu, L., Gandhi, P., Inada, N., et al. 2013, ApJ, 767, 157
Guo, F., & Mathews, W. 2010, ApJ, 717, 937
Guo, F., Oh, S. P., & Ruszkowski, M. 2008, ApJ, 688, 859
Henning, J., Gantner, B., Burns, J., et al. 2009, ApJ, 697, 1597
Hudson, D. S., Mittal, R., Reiprich, T. H., et al. 2010, A&A, 513, 37
Humphrey, P., Liu, W., & Buote, D. 2009, ApJ, 693, 822
Humphrey, P. J., Buote, D. A., Brighenti, F., et al. 2012, ApJ, 748, 11
Lin, Y., & Mohr, J. 2004, ApJ, 617, 879
Mahdavi, A., & Geller, M. J. 2004, ApJ, 607, 202
Mahdavi, A., Hoekstra, H., Babul, A., et al. 2013, ApJ, 767, 116
Massey, R., Williams, Li., Smit, R., et al. 2015, MNRAS, 449, 3393
Matsushita 2011, A&A, 537, A134
Maughan, B. J., Giles, P. A., Randall, S., et al. 2012, MNRAS, 421, 1583
McGlynn, T., & Fabian, A. 1984, MNRAS, 208, 709
McMullin, J. P., Waters, B., Schiebel, D., et al. 2007, in ASP Conf. Ser. 376, Astronomical Data Analysis Software and Systems XVI, ed. R. A. Shaw, F. Hill, & D. J. Bell (San Francisco, CA: ASP), 127
McNamara, B. R., & Nulsen, P. E. J. 2007, ARA&A, 45, 117
Million, E., Werner, N., Simionescu, A., et al. 2011, MNRAS, 418, 2744
Molendi, S., & Pizzalato, F. 2001, ApJ, 560, 194
Motl, P., Burns, J. O., Loken, C., et al. 2004, ApJ, 606, 635
Quintana, H., & Ramirez, A. 1995, ApJS, 96, 343
Randall, S., Nulsen, P., Forman, W. R., et al. 2008, ApJ, 688, 208
Rasia, E., Borgani, S., Murante, G., et al. 2015, ApJ, 815, 17L
Read, J. I., Goerdt, T., & Moore, B. 2006, MNRAS, 373, 1451
Revnivtsev, M., Churazov, E., Sazonov, S., et al. 2008, A&A, 490, 37
Rossetti, & Molendi 2010, A&A, 510, A83
Russell, H., Fabian, A., McNamara, B., et al. 2014, MNRAS, 444, 629
Sanders, J., Fabian, A., & Allen, S. 2004, MNRAS, 349, 952
Sanders, J. S. 2006, MNRAS, 371, 829
Sanderson, A., O'Sullivan, E., & Ponman, T. 2009, MNRAS, 395, 764
Sanderson, A., & Ponman, T. 2010, MNRAS, 402, 65
Sanderson, A., Ponman, T., & O'Sullivan, E. 2006, MNRAS, 372, 1496
Simionescu, A., Werner, N., Forman, W. R., et al. 2010, MNRAS, 405, 91
Skrutskie, M. F., Cutri, R. M., Stiening, R., et al. 2006, AJ, 131, 1163
Smith, R. K., Brickhouse, N. S., Liedahl, D. A., & Raymond, J. C. 2001, ApJL, 556, L91
Su, Y., Buote, D., Gastaldello, F., et al. 2015, ApJ, 805, 104
Su, Y., Gu, L., White, R., et al. 2014, ApJ, 786, 152
Su, Y., & Irwin, J. 2013, ApJ, 766, 61
Su, Y., Irwin, J., White, R., et al. 2015, ApJ, 806, 156
Vikhlinin, A., Kravtsov, A., Forman, W., et al. 2006, ApJ, 640, 691
Voigt, L. M., & Fabian, A. C. 2004, MNRAS, 347, 1130
Voit, G. M., Cavagnolo, K. W., Donahue, M., et al. 2008, ApJ, 681, 5L
Werner, N., Urban, O., Simionescu, A., et al. 2013, Natur, 502, 656
Wu, X., Xue, Y., & Fang, L. 1999, ApJ, 524, 22